

# Image-based Study of Wave Characteristics over Shallow Fringing Reef

Weijie LIU<sup>1</sup>, Yoshimitsu TAJIMA<sup>2</sup> and Takenori SHIMOZONO<sup>3</sup>

<sup>1</sup>Doctoral Student, Dept. of Civil Eng., The University of Tokyo  
(Hongo 7-3-1, Bunkyo-ku, Tokyo 113-8656, Japan)  
E-mail: magiclwj@coastal.t.u-tokyo.ac.jp

<sup>2</sup>Member of JSCE, Professor, Dept. of Civil Eng., The University of Tokyo  
(Hongo 7-3-1, Bunkyo-ku, Tokyo 113-8656, Japan)  
E-mail: yoshitaji@coastal.t.u-tokyo.ac.jp

<sup>3</sup>Member of JSCE, Assistant Professor, Dept. of Civil Eng., The University of Tokyo  
(Hongo 7-3-1, Bunkyo-ku, Tokyo 113-8656, Japan)  
E-mail: shimozono@coastal.t.u-tokyo.ac.jp

This study aims to investigate the characteristic behavior of severe wave inundation along the reef coast during typhoon event. Laboratory experiments were performed to represent storm waves transforming over shallow fringing reef. Image-based measuring technique was developed and applied to capture the wave characteristics as high-resolution data sets both in spatial and temporal domains. It was found through the obtained experimental data set that, besides significantly elevated mean water level, infragravity waves were generated and formed standing waves on the reef even though regular periodic waves were introduced to the flume. Amplitude of the observed resonant infragravity wave was highly dependent on the period of incident regular waves. Wave-induced radiation stress near the breaking point also had fluctuations with frequency of infragravity waves and the phase of this fluctuating radiation stress matched with that of estimated acceleration of horizontal velocity at the node of observed resonant infragravity waves. This wave-induced radiation stress near the breaking point may also change the period of infragravity wave or even vanish the evolutions of infragravity waves.

**Key Words:** *fringing reef, inundation, infragravity wave, radiation stress, wave breaking*

## 1. INTRODUCTION

Fringing reefs are shore-attached reefs characterized by shallow platforms that drop off sharply into deep water. The typhoon Haiyan hit the Philippines in November 2013 and caused severe damages along its long coastline. The coast of the Eastern Samar fronted by fringing reefs was one of the coasts which suffered significantly high inundation due to storm waves caused by typhoon Haiyan<sup>1)</sup>. Field observations revealed that maximum runup heights of over 10 m were distributed along the coast in spite of wave dissipation due to strong breaking over the steep foreface of the reef. Similar extensive damage has also been reported in low-lying coastal areas fronted by coral reefs during past typhoon events<sup>2)</sup>.

The goal of this study is to investigate the characteristics behavior of such large inundation that eventually cause severe damages along the coasts with fringing reef.

In this study, laboratory experiments are conducted in the wave flume with a fringing reef system based on the bathymetry of Eastern Samar coast. Incident regular waves with different periods are generated by the wave maker. Image-based measuring system is then developed and applied to capture the wave characteristics over the whole fringing reef system with high resolutions both in time and space domains. Finally, the high-resolution data sets are analyzed to further deduce the physical mechanism of the high inundation at shoreline by comparing different wave cases.

## 2. LABORATORY EXPERIMENT

Laboratory experiments were conducted to represent storm waves transforming over the fringing reef. Image-based measuring system was developed and applied to capture the wave characteristics over

the whole fringing reef system with high resolutions both in time and space domains.

### (1) Experimental setups

**Fig.1** shows the schematic view of the experimental setups. A physical model of fringing reef was made in a 30m-long and 60cm-wide wave flume. The reef cross section consists of a 1:13.3 sloping beach, a 1.92m-wide reef flat and a 1:7 steeper reef face. The still water depth over the reef flat was 1cm. Wave gauge was installed in front of the wave maker to measure the incident wave heights. Three JVC HD cameras with a frame rate of 30 fps, recorded successive still images of water surface along the whole reef cross section in which the water and background were colored in blue and yellow, respectively. Two spotlights were used to light up the measuring area. In order to synchronize three cameras, two spotlights were turned on after the initiation video recording in each experimental case.

### (2) Image-based data acquisition system

The recorded video images were converted to still images of each frame with high resolution pixel size of 1/1920m. Obtained images were first rectified based on the actual XY-square coordinate system on the glass wall of the flume. Eight reference points with known XY-square-coordinates on the glass wall were applied for this rectification. Rectification parameters, such as camera locations, angles, focal length and lens distortion, were estimated so that these parameters yield the minimum root-mean-square errors of estimated pixel coordinates at eight reference points with known coordinates<sup>3)</sup>.

The instantaneous surface water fluctuations over the reef system were estimated from the rectified still images. Based on the RGB-values in each pixel, the surface water boundary over the reef system was detected through the following parameter,

$$A = R + G - B \quad (1)$$

Yellow color has larger values of both  $R$  and  $G$  while blue color has larger  $B$  but smaller values of  $R$  and  $G$ . Computed  $A$  in Eq.(1) therefore should have larger value on the yellow background and smaller value on the blue water and should therefore be decreased abruptly at the air-water boundary. Under the present experimental setup,  $A$  was always greater than 200 on the yellow background while it was always less than 100 on the blue water even at the surface of broken waves where the water color tended to be brighter than elsewhere. This study therefore determined the surface water boundary condition of  $A$  by a single critical value,  $A=150$ , which is just between 200 and 100. Starting from the arbitrary points on

the yellow background, the system search the pixel location in the vertical downward direction until  $A$  first goes below the critical value,  $A=150$ . Detected pixel coordinates at the water surface boundary were then transferred to the actual XY-coordinates on the glass wall of the flume. Estimated error of the rectified coordinates of the still water level, which are defined to be zero for the present rectification, was less than 1mm.

## 3. RESULTS AND DISCUSSIONS

All the incident waves broke violently on the steep reef face and showed plunging breaker type behavior with a big splash. **Table 1** shows the experimental wave cases and the primary results estimated from the image-based measuring system. In the table,  $H_i$  and  $T_i$  are the incident wave height and period,  $T_L$  and  $H_L$  are period and height of the surface water fluctuations of infragravity wave components, and  $\eta_{avg}$  and  $\eta_{max}$  are the mean water level and the largest inundation height near the shoreline where is 1.82m away from the reef edge. As summarized in this table, incident regular wave heights were nearly the same, i.e., around 11cm, in all the cases while incident wave period of each case ranges from 1.2s to 1.9s.

**Fig.2 (a)** shows the examples of observed surface water fluctuations near the shoreline when waves with shorter incident periods of  $T_i=1.2s$  or  $T_i=1.5s$  were introduced. **Fig.2 (b)** shows the similar surface water fluctuations when waves with longer incident periods of  $T_i=1.8s$  or  $T_i=1.9s$  were introduced. The figure shows the water surface fluctuations for 60

**Table 1** List of experimental wave cases and primary results.

Case No.	$H_i$ (cm)	$T_i$ (s)	$\eta_{avg}$ (cm)	$T_L$ (s)	$H_L$ (cm)	$\eta_{max}$ (cm)
1	11.2	1.2	3.6	11.37	2.5	5.9
2	10.8	1.4	4.0	11.37	3.2	7.3
3	11.4	1.5	4.3	11.37	3.5	8.2
4	11.8	1.8	4.4	8.53	3.5	8.4
5	11.6	1.9	4.5	—	—	6.3

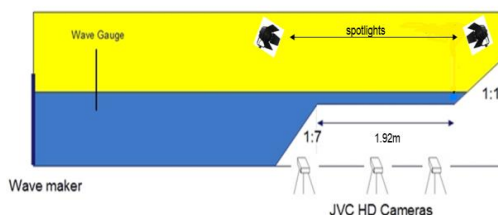


**Fig.1** Schematic view of the experimental setups

seconds after it reached periodic equilibrium state. Following subsections discuss characteristic features of observed surface water fluctuations.

### (1) Power spectrum of surface fluctuations

As seen in **Table 1** and **Fig.2**, the mean water level is elevated and stays around 4cm above the still water level in all the cases. Besides the elevated mean water level and fluctuations due to incident waves, the observed surface water fluctuations clearly contain low frequency infragravity wave components except the wave case with incident period of 1.9s. The cross-shore distribution of power spectrum of obtained surface fluctuations are shown in **Fig.3** for all the wave cases. In **Fig.3**, origin of the horizontal axis is set 88cm seaside from the reef edge and the vertical axis is the frequency,  $f$ . As seen in the figure, in the wave cases with shorter incident periods of 1.2s, 1.4s, 1.5s, the low frequency infragravity waves dominate the wave motion near the shoreline, i.e.,  $X > 200$ cm, and have the same period,  $T_L = 11.37$ s. In the wave case with longer period of 1.8s, on the other hand, the period of dominant infragravity wave near shoreline decreases to 8.53s and in the wave case of 1.9s, the low frequency infragravity waves nearly vanish.

### (2) Phase relationship of infragravity waves

In order to further investigate the characteristic behavior of observed infragravity waves, this study compared the phase relationships through the following analysis. The normalized cross-correlation,  $R_{l2}$ , between the time series of infragravity component near the shoreline where is 1.82m away from the reef edge,  $\eta_{l1}(t)$ , and the one at arbitrary location inside and outside of the reef,  $\eta_{l2}(t, x)$ , was estimated by the following formulae,

$$R_{l2}(\tau, x) = \frac{E[(\eta_{l1}(t) - E(\eta_{l1}(t))) (\eta_{l2}(t + \tau, x) - E(\eta_{l2}(t, x)))]}{\sigma_{\eta_{l1}} \sigma_{\eta_{l2}}} \quad (2)$$

where  $\tau$  is the time shifted,  $E(\quad)$  denotes the time-average over the entire time-series of the data,  $\sigma_{\eta_{l1}}$  and  $\sigma_{\eta_{l2}}$  are the standard deviations of  $\eta_{l1}$  and  $\eta_{l2}$ , respectively. Filtered surface water fluctuations of observed infragravity components were obtained through Fourier transform with frequency components around  $T_L = 11.37$ s for cases of  $T = 1.2$ s, 1.4s and 1.5s and around  $T_L = 8.53$ s for the case of  $T = 1.8$ s, respectively. **Fig.4** shows the cross-shore distributions of  $R_{l2}$  for the wave cases with incident periods of 1.2s, 1.4s, 1.5s and 1.8s. As shown in Eq.(2),  $R_{l2}$  is obtained as functions of  $x$  and  $\tau$  and the vertical axis in **Fig.4** denotes the phase gap,  $\Delta\phi = 2\pi\tau/T_L$ . Horizontal axis in **Fig.4** is the cross-shore location and is the same as the one in **Fig.3**.

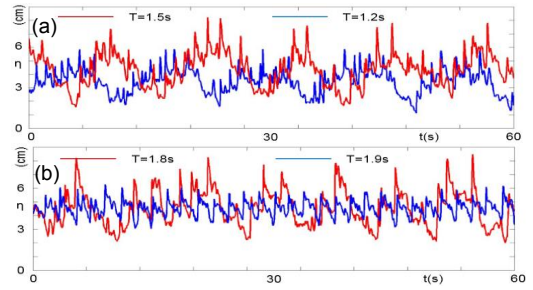


**Fig.2** Time series of water surface fluctuations near the shoreline when the period of incident waves are: 1.2s (top, blue), 1.5s (top, red), 1.8s (bottom, red) and 1.9s (bottom, blue), respectively.

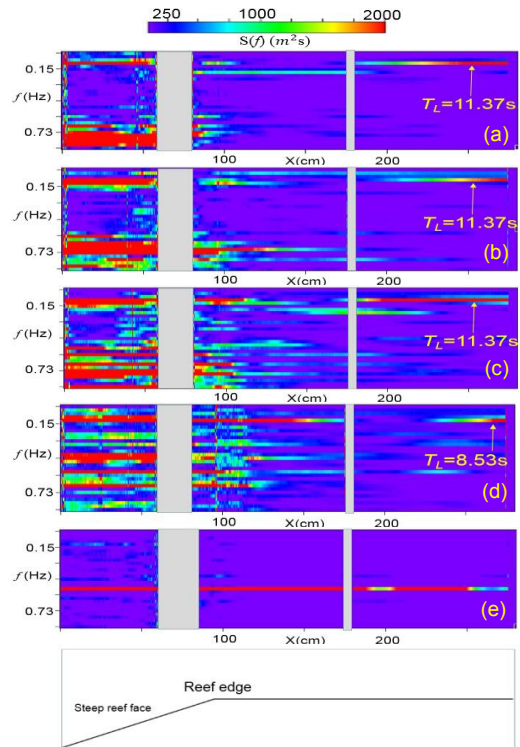


**Fig.3** Cross-shore distribution of power spectrum of observed surface fluctuations for the wave cases of (a)  $T_i = 1.2$ s, (b)  $T_i = 1.4$ s (c)  $T_i = 1.5$ s and (d)  $T_i = 1.8$ s (e)  $T_i = 1.9$ s.

In the figure, the profile of  $\eta_{l2}$  at arbitrary cross-shore location best match with the profile near the shoreline,  $\eta_{l1}$ , where estimated  $R_{l2}$  reaches its peak. As seen in **Fig.4**, in the wave cases with shorter incident period of 1.2s, 1.4s and 1.5s, the peak of  $R_{l2}$  is observed near  $\Delta\phi = 0$  in the cross-shore range of  $X > 150$ cm whereas the peak is located near  $\Delta\phi = \pi$  at  $X < 130$ cm. This observed phase relationship surely indicates that the infragravity wave formed similar

standing waves with the node located between  $X=130\text{cm}$  and  $X=150\text{cm}$  in these three relatively shorter wave cases.

In the wave case of  $T_i=1.8\text{s}$ , on the other hand, the peak of  $R_{12}$  is observed near  $\Delta\phi=0$  at  $X>200\text{cm}$  whereas the peak is located near  $\Delta\phi=\pi$  at  $X<180\text{cm}$ , which indicates that the infragravity wave also formed standing wave while the position of node is located between  $X=180\text{cm}$  and  $X=200\text{cm}$ , different from the wave cases with shorter incident period.

### (3) Fluctuation of wave radiation stress

As seen in Table 1 and Fig.2, the height of surface water fluctuations of the infragravity wave components were relatively larger in the case of  $T_i=1.4\text{s}$ ,  $T_i=1.5\text{s}$  and  $T_i=1.8\text{s}$  rather than that of  $T_i=1.2\text{s}$  and thus the case of  $T_i=1.4\text{s}$ ,  $T_i=1.5\text{s}$ , and  $T_i=1.8\text{s}$  showed higher inundation near the shoreline.

Further analysis was carried out to explore the physical mechanism of how observed infragravity waves were amplified by waves with some specific period. Fig.5 shows examples of the temporal and spatial distribution of the standard deviation of the surface water fluctuation,  $\eta_{rms}$ , obtained from each wave period of the incident wave case of  $T_i=1.5\text{s}$  and  $T_i=1.8\text{s}$ . As seen in the figure, periodic variations of  $\eta_{rms}$  are observed along the solid line AA, denoting the location of reef edge. This feature clearly suggests that the breaking point of incident wave on the steep reef face has certain periodic oscillation and thus the associated radiation stress should also have corresponding fluctuations.

Phase-averaged horizontal momentum equation is expressed as

$$\rho D \frac{\partial U_L}{\partial t} = -\frac{\partial S_{xx}}{\partial x} - \rho g D \frac{\partial \eta_L}{\partial x} \quad (3)$$

where  $U_L$  is horizontal velocity of low-frequency components,  $S_{xx}$  is wave radiation stress,  $D$  is water depth and  $\eta_L$  is the low-frequency components of water surface level fluctuations. As seen in Eq.(3), acceleration of the horizontal current velocity,  $U_L$ , is determined as a force balance of radiation stress and slowly varying hydrostatic pressure gradient. Low-frequency fluctuations should therefore be amplified if the phase of fluctuating wave radiation stress matches with that of fluctuating acceleration of horizontal velocity components and should be attenuated if vice versa.

As seen in Fig.4 and Fig.5, incident waves are broken at the seaside of the first node from the shoreline and, since the observed infragravity wave components formed standing waves, the phase difference of low-frequency components of water surface fluctuations near the shoreline,  $\eta_{L1}$ , and the

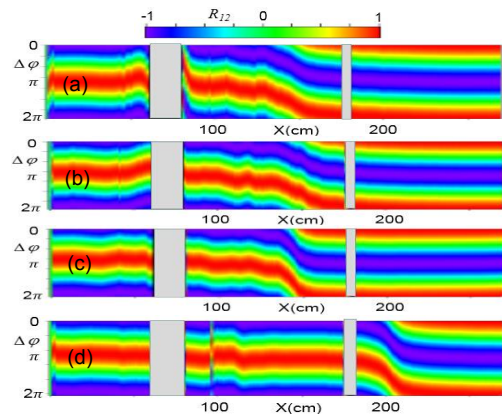


Fig.4 Cross-shore distribution of cross-correlation, as a function of the phase gap, of the filtered infragravity waves for the wave cases of (a)  $T_i=1.2\text{s}$ , (b)  $T_i=1.4\text{s}$  (c)  $T_i=1.5\text{s}$  and (d)  $T_i=1.8\text{s}$ .

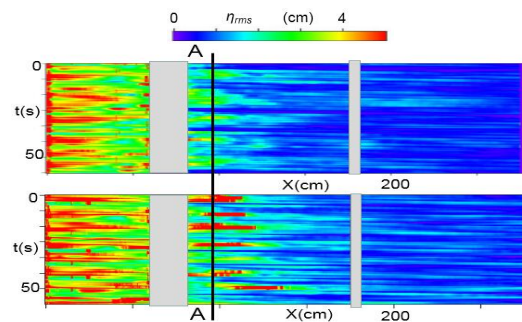


Fig.5 Temporal and spatial distribution of the standard deviation of the surface water fluctuations for the incident wave cases of  $T_i=1.5\text{s}$  (top) and  $1.8\text{s}$  (bottom)

Table 2 List of  $R_{max}$  between the fluctuating radiation stresses near the breaking point and the infragravity surface oscillation near the shoreline and corresponding  $\Delta\phi$  for wave cases of  $T_i=1.2\text{s}$ ,  $1.4\text{s}$ ,  $1.5\text{s}$  and  $1.8\text{s}$

Case No.	$T_i$ (s)	$R_{max}$	$\Delta\phi$
1	1.2	0.76	$0.12\pi$
2	1.4	0.37	$1.3\pi$
3	1.5	0.30	$1.2\pi$
4	1.8	0.32	$0.87\pi$

acceleration of shoreward horizontal velocity under the broken waves should be  $\pi$ . Standing waves therefore maybe amplified if the phase difference between  $\eta_{L1}$  and fluctuating wave radiation stress is around  $\pi$ . Since low-frequency components of the horizontal velocity under the broken waves are not recorded, this study compared the phase relationship between oscillating profiles of  $\eta_{L1}$  and wave radiation stress near the breaking point.

Under the linear shallow water theory, wave ra-



diation stress is proportional to the wave energy. This study thus simply determined the profile of the fluctuating wave radiation stress near breaking point by:

$$-\frac{\partial S_{xx}}{\partial x} \propto -\frac{(\eta_{A,rms}^2(t) - \eta_{B,rms}^2(t))}{L} = f(t) \quad (4)$$

with  $\eta_{A,rms1}(t)$  and  $\eta_{B,rms2}(t)$ , time-varying standard deviation of the surface water fluctuations respectively at seaside and shoreside of the breaking point, i.e., the one at 8.3cm seaside and the other at 4.2cm shoreside from the reef edge, and with  $L = 12.5\text{cm}$ , the horizontal distance of these two locations.

Replacing  $\eta_{L2}(t)$  by  $f(t)$  in Eq.(2), cross-correlation of wave radiation stress and time-varying infragravity fluctuations near the shoreline can be computed as a function of phase gap,  $\Delta\phi$ . **Table 2** summarizes the peak value of cross-correlation,  $R_{\max}$ , and corresponding phase gap,  $\Delta\phi$ , for each incident wave cases of  $T_i=1.2\text{s}$ ,  $1.4\text{s}$ ,  $1.5\text{s}$  and  $1.8\text{s}$ . As seen in **Table 2**, estimated phase gap was around zero in the case of  $T_i=1.2\text{s}$  whereas it was around  $\pi$  in the case of  $T_i=1.4\text{s}$ ,  $1.5\text{s}$  and  $1.8\text{s}$ . Generated infragravity waves therefore may be further amplified in the cases of  $T_i=1.4\text{s}$ ,  $1.5\text{s}$  and  $1.8\text{s}$  and this feature is consistent with the observed height of infragravity waves, i.e., as summarized in **Table 1**,  $H_L$  in the cases of  $T_i=1.4\text{s}$ ,  $1.5\text{s}$  and  $1.8\text{s}$  were larger than that of  $T_i=1.2\text{s}$ . **Fig.6** shows the examples of the profiles of the time series of  $\eta_{L1}(t)$  and  $f(t)$  for the wave case of  $T_i=1.2\text{s}$  and  $T_i=1.5\text{s}$ , respectively. Contrast of the phase relationship between  $\eta_{L1}$  and  $f(t)$  in these two wave cases can be clearly seen in the figure.

As seen in Fig.5, penetration distance of breaking and broken waves beyond the edge of coral reef was longer in the case of  $T_i=1.8\text{s}$  rather than the one of  $T_i=1.5\text{s}$ . These characteristics of breaking waves may determine the frequency of resonant infragravity wave components and the corresponding node position developed on the reef.

In the wave case of  $1.9\text{s}$ , it was found the incident wave breaking point was much steadier than other cases during the experiment and this may be because incident wave period,  $T_i=1.9\text{s}$ , is no longer short enough compared to the period of infragravity waves which could form resonant standing waves on the limited width of the coral reef. Since the infragravity waves could not form resonant standing waves, wave breaking points and heights are more stabilized. Stabilized wave radiation stress also stabilize the wave setup and enhance vanishment of the infragravity oscillations on the reef.

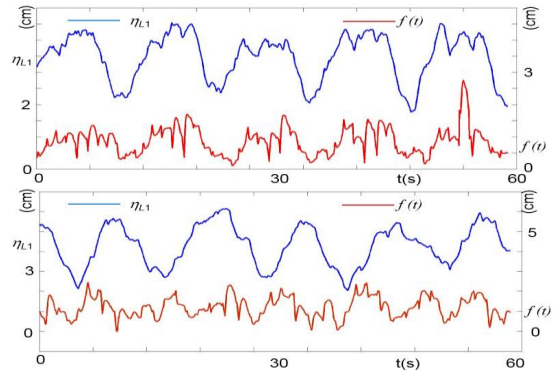


**Fig.6** Profiles of the time series of infragravity component near the shoreline,  $\eta_{L1}$  (blue), and the profiles of the wave radiation stress near breaking point,  $f(t)$  (red), for the wave case of  $T_i=1.2\text{s}$  (top) and  $T_i=1.5\text{s}$  (bottom)

#### 4. CONCLUSIONS

Image-based measuring system was developed and successfully applied to the experiments to capture the wave characteristics with high spatial and temporal resolutions over a typical fringing reef in the wave flume. Through the experiments, high mean water level were observed near shoreline in all wave cases. Resonant infragravity waves and the node position on the reef were clearly revealed by analysis of the high-resolution data. It was also found that larger inundation happened in some wave cases when the fluctuating radiation stress near breaking point has more impact on amplification of the surface water fluctuations of infragravity wave components near the shoreline.

The effect of the radiation stress near breaking point may also change the period of the infragravity component and even cause the vanishment of the low frequency oscillation.

#### REFERENCES

- 1) Tajima, Y., Yasuda, T., Pacheco, B.M., Cruz, E. C., Kawasaka, K., Nobuoka, H., Miyamoto, M., Asano, Y., Ari-kawa, T., Ortigas, N.M., Aquino, R., Mata, W., Valdez, J. and F. Briones: Initial report of JSCE-PICE Joint Survey on the storm surge disaster caused by Typhoon Haiyan, Coastal Eng. Journal, World Scientific, DOI: 10.1142/S0578563414500065, 2014.
- 2) Nwogu, Z. : Infragravity wave motions and runup over shallow fringing reefs, *J. Waterway, Port, Coastal, and Ocean Engineering*, Vol. 136, No. 6, pp. 295-305, 2010.
- 3) Tajima, Y. and S. Sato: Local concentration of slowly varying wave and current fields around the abruptly changing bottom slopes along the shore, *Proc. of 32nd Int. Conf. on Coastal Engineering*, 2010.